ECS Journal of Solid State
Science and Technology

OPEN ACCESS

Properties of Atomic Layer Deposited Nanolaminates of Zirconium and Cobalt Oxides

To cite this article: Helina Seemen *et al* 2018 *ECS J. Solid State Sci. Technol.* **7** P402

View the article online for updates and enhancements.

This content was downloaded from IP address 157.88.20.207 on 08/01/2021 at 10:47

Properties of Atomic Layer Deposited Nanolaminates of Zirconium and Cobalt Oxides

Helina Seemen,[1,z] Mihkel Rähn,[1] Kristjan Kalam,[1] Timo Sajavaara,[2] Salvador Dueñas,[3] Helena Castán,[3] Joosep Link,[4] Raivo Stern,[4] Kaupo Kukli,[1,5] and Aile Tamm[1]

[1]Institute of Physics, University of Tartu, 50411 Tartu, Estonia
[2]Department of Physics, University of Jyväskylä, 40500 Jyväskylä, Finland
[3]Department of Electronics, University of Valladolid, 47011 Valladolid, Spain
[4]National Institute of Chemical Physics and Biophysics, 12618 Tallinn, Estonia
[5]Department of Chemistry, University of Helsinki, FI-00014 Helsinki, Finland

Five-layer crystalline thin film structures were formed, consisting of ZrO_2 and Co_3O_4 alternately grown on Si(100) substrates by atomic layer deposition at 300°C using $ZrCl_4$ and $Co(acac)_3$ as the metal precursors and ozone as the oxygen precursor. The performance of the laminate films was dependent on the relative content of constituent oxide layers. The magnetization in these films was nonlinear, saturative, and with very weak coercive fields. Electrical measurements revealed the formation of significant polarization versus external field loops and implied some tendency toward memristive behavior.
© The Author(s) 2018. Published by ECS. This is an open access article distributed under the terms of the Creative Commons Attribution 4.0 License (CC BY, http://creativecommons.org/licenses/by/4.0/), which permits unrestricted reuse of the work in any medium, provided the original work is properly cited. [DOI: 10.1149/2.0191808jss]

Manuscript submitted June 11, 2018; revised manuscript received July 19, 2018. Published July 28, 2018.

Co_3O_4 and ZrO_2 thin films and their nanolaminates are of interest as functional thin films possessing advanced electronic, optical, magnetic and mechanical properties, making these materials attractive for several applications.

ZrO_2 can be used in gas sensors,[1,2] catalytic supports,[3,4] thermal barrier coatings,[5,6] buffer layers for superconductors[7,8] and as dielectric material in dynamic random access memory (DRAM)[9–13] and resistive random access memory (RRAM) devices.[14,15]

Co_3O_4 has been investigated as a gas sensor,[16,17] catalyst,[18,19] anode material for lithium-ion batteries,[20] supercapacitor electrode,[21] superhydrophobic coating,[22,23] and magnetic semiconductor.[24] Co_3O_4 has also demonstrated resistive switching properties, which are important regarding its potential applications in RRAM devices.[25,26]

Co_3O_4 and ZrO_2 oxides may be grown using different physical and chemical techniques, such as solution spray pyrolysis,[27–29] chemical vapor deposition,[30–33] pulsed laser deposition,[34,35] sol-gel,[36,37] electron-beam evaporation,[38,39] or, atomic layer deposition (ALD).[40–46] Herewith, ALD may be regarded as the ultimate method providing the most precise thickness control over large substrate areas.

ZrO_2 has been used in nanolaminates as one alternating component together with, e.g., Al_2O_3,[47–50] SiO_2,[51] Ta_2O_5,[52,53] HfO_2,[53,54] Er_2O_3,[55] Gd_2O_3,[56] and Y_2O_3.[57] Studies on nanolaminates or multilayered structures containing Co_3O_4 as one of the constituents[58,59] as well as ALD-grown nanolaminates containing both Co_3O_4 and ZrO_2[59] have so far been quite scarce. In the earlier study devoted to ZrO_2-Co_3O_4 nanocomposites grown by ALD using the same chemistry based on cobalt acetylacetonate, zirconium tetrachloride and ozone,[59] the deposition process for cobalt oxide was investigated and established, determining suitable evaporation temperature for $Co(acac)_3$ precursor, as well as by recording linear relationship between growing mass and the amount of deposition cycles. Using the suitable deposition parameters, ALD growth of ZrO_2/Co_3O_4 double layers was demonstrated, together with their performance as dielectric and magnetic materials.

In connection with the demand for materials, which could be applied in novel memories because of their advanced magnetic and electric properties, this study was devoted to the description of ZrO_2-Co_3O_4 nanolaminates, grown by ALD using $ZrCl_4$ and $Co(acac)_3$ as the metal precursors and ozone as the oxygen precursor. Elemental and phase composition, thickness, surface morphology and the polarization characteristics of the samples in the presence of an external magnetic or electric field were determined. In addition, the resistive switching and other electrical characteristics of ZrO_2-Co_3O_4 nanolaminates were studied to evaluate whether such films can imply a tendency toward memristive behavior.

Experimental

The film growth experiments were carried out in a flow-type in-house built hot-wall ALD reactor[60] at 300 ± 2°C using $ZrCl_4$ (99.99%, Sigma Aldrich) and $Co(acac)_3$ (99.9%, Volatec Ltd.) [acac = tris(2,4-pentanedionato)] as the metal precursors, O_3 as the oxygen precursor and N_2 (99.999%, AGA) as the carrier and purge gas. The $ZrCl_4$ and $Co(acac)_3$ were evaporated at 160 ± 2°C and 120 ± 2°C, respectively, from open boats inside the reactor and transported to the substrates by the carrier gas flow. O_3 was generated from O_2 (99.999%, AGA, Linde Group) in a BMT Messtechnik 802 N ozone generator. The O_3 concentration output of the generator measured with BMT Masstechnik 964 analyzer was ~262 g/m^3 at the normal pressure. During the deposition, the chamber pressure varied in the range of 205–260 Pa. In all cases, a single ALD cycle was started with a metal precursor pulse and continued with a purge of the reaction zone with the pure carrier gas, oxygen precursor pulse and another purge. The precursor pulse durations and purge lengths in the case of ZrO_2 reference films were 5-5-5-5 s and in the case of Co_3O_4 reference films were 5-3-5-5 s, denoting the sequence of metal precursor pulse – N_2 purge – O_3 pulse – N_2 purge. The number of cycles for both reference films was 250. In the case of the nanolaminates, the precursor pulse durations and purge lengths were 5-5-5-5 s and 7-5-5-5 s for ZrO_2 and Co_3O_4, respectively. The $Co(acac)_3$ pulse time was prolonged by 2 seconds during the deposition of the layered structures, in order to ensure more uniform adsorption of precursor molecules and deposition of the oxide more evenly along the gas flow. ZrO_2-Co_3O_4 nanolaminates consisting of 5 alternating layers starting with ZrO_2 layer and ending, again, with ZrO_2 as the topmost layer were grown using the total sequence of $2 \times [(100 \times (ZrCl_4/O_3) + 200 \times (Co(acac)_3/O_3)] + 100 \times (ZrCl_4/O_3)$ cycles. The abbreviation $2 \times (ZrO_2 + Co_3O_4) + ZrO_2$ will be used throughout the article for indicating that nanolaminate. The nanolaminates starting with Co_3O_4 layer and ending also with Co_3O_4 as the topmost layer were grown using the total sequence of $2 \times [(200 \times (Co(acac)_3/O_3) + 100 \times (ZrCl_4/O_3)] + 200 \times (Co(acac)_3/O_3)$ cycles. This particular laminate will further be denoted as $2 \times (Co_3O_4 + ZrO_2) + Co_3O_4$, throughout the paper. Pieces of undoped Si(100) wafers as well as highly-doped Si covered by TiN layer were exploited as substrates. TiN layer was deposited using $TiCl_4/NH_3$ process in an ASM A412 Large Batch 300 mm reactor at Fraunhofer IPMS-CNT.

[z]E-mail: helina.seemen@ut.ee

Table I. Thickness and growth rate data of the ZrO_2 and Co_3O_4 reference thin films and ZrO_2-Co_3O_4 nanolaminates deposited on Si substrate.

	Co_3O_4	ZrO_2	$2 \times (Co_3O_4 + ZrO_2) + Co_3O_4$		$2 \times (ZrO_2 + Co_3O_4) + ZrO_2$	
Total thickness, nm (XRF)	15.6 ± 1.0	32.9 ± 1.0	64.0 ± 1.0		59.7 ± 1.0	
Total thickness, nm (XRR)	15.0 ± 1.0	32.0 ± 1.0				
Total thickness, nm (ellipsometry)	17.4 ± 1.0	29.9 ± 1.0				
			Co_3O_4	ZrO_2	Co_3O_4	ZrO_2
No. of ALD cycles for 1 layer	250	250	200	100	200	100
Total thickness of specified oxide, nm (XRF)			41.9 ± 1.0	22.1 ± 1.0	25.6 ± 1.0	34.1 ± 1.0
Estimated thickness of a single oxide layer, nm (XRF)			14.0 ± 2.0	11.1 ± 2.0	12.8 ± 2.0	11.4 ± 2.0
Growth rate, nm/cycle	0.06	0.13	0.21	0.22	0.13	0.34

In the case of undoped Si(100), the native SiO_2 was removed using HF. The conducting substrates were based on (100)-oriented silicon with resistivity in the range of 0.014–0.020 $\Omega \cdot$ cm, i.e., boron-doped to concentrations up to 5×10^{18}–1×10^{19}/cm^3, and coated with 10 nm thick chemical vapor deposited titanium nitride layer.

The mass thickness and elemental composition of the films were measured by X-ray fluorescence (XRF) spectroscopy method using ZSX400 (Rigaku) spectrometer. Grazing incidence X-ray diffraction (GIXRD) was applied for structural studies and all XRD studies were carried out with Smartlab (Rigaku) X-ray analyzer using CuKα radiation. Thicknesses of the ZrO_2 and Co_3O_4 reference films were determined using GES5E (Sopra-Semilab) spectroscopic ellipsometer. The composition profile of selected films, including the detection and determination of the content of light residues such as hydrogen, carbon and nitrogen, was evaluated by time-of-flight elastic recoil detection analysis (ToF-ERDA). ToF-ERDA was carried out using 11.915 MeV $^{63}Cu^{7+}$ ion beam. The geometry used for measurements was $10^\circ + 31^\circ$.

The morphology of nanolaminates on Si substrate was investigated by scanning electron microscopy (SEM) using FEI Helios Nanolab 600 DualBeam microscope equipped with focused ion beam (FIB) module and Omniprobe model 100.7 in-situ nanomanipulator. Ga FIB was employed for the preparation of the lamellae of the ZrO_2-Co_3O_4 nanolaminates, being used for milling, thinning and polishing. The nanomanipulator was used for transportation of the lamellae to the lift-out type grid and Pt deposition was used for lamellae attachment steps. Before the start of the milling process, small ($\sim 20 \times 1$ μm) and thin ($\sim$1 μm) rectangular shaped C and Pt layers were deposited on top of the object using electron beam (for the first C and Pt layers) and Ga ion beam (the last Pt layer) to protect the area of interest during the lamella creation process. For that, the gas compound, which was naphthalene [$C_{10}H_8$] for C deposition and methyl cyclopentadienyl trimethyl platinum [$(CH_3)_3Pt(CpCH_3)$] for Pt deposition, was exposed onto the target specimen, using the gas injection nozzle, and adsorbed on specimen's surface. This was followed by bombardment of focused beam on the adsorbed molecules within predefined patterns. After that routine milling process, lamellae transportation and attachment to the lift-out type TEM grid, final thinning and polishing process were completed. Lamella creation is one necessary preparation step to change a thin film object into a suitable form for transmission electron microscopy (TEM) studies. This lamella stores information about the cross-sectional structure and composition of the object.

Scanning transmission electron microscopy (STEM) studies for the characterization of the cross-sections of the nanolaminate structures were carried out using FEI Titan Themis 200 instrument with a field emission gun operated at 200 kV. The device was equipped with a probe C_s corrector and a Bruker SuperX SDD Energy-dispersive X-ray spectroscopy (EDX) system. The EDX system was used for the composition profiling of the ZrO_2-Co_3O_4 nanolaminates.

Selected films were subjected to magnetic measurements. The measurements were performed using the P525 Vibrating Sample Magnetometer (VSM) option of the Physical Property Measurement System (PPMS) 14T (Quantum Design). Rectangular samples with the area of ca. 14.4 ± 0.7 mm^2 were fixed with GE 7031 vanish to the commercial quartz sample holders (Quantum Design). Hysteresis measurements were carried out at room temperature (300 K) by scanning the magnetic fields from −5000 to +5000 Oe (from −397.9 to 397.9 kA/m) parallel to the film surface. The diamagnetic signal arising from the silicon substrate was subtracted from the general magnetization curve for all the samples in which the ferromagnetic like response was detected.

In order to carry out the electrical measurements, metal-insulator-metal (MIM) structures were prepared on conducting substrates. Top electrodes with area of 0.204 mm^2 were formed by electron beam evaporation of 50 nm thick Pt layers directly contacting ZrO_2-Co_3O_4 nanolaminates through a shadow mask. Capacitance-voltage (C–V) and current-voltage (I–V) measurements were carried out in a light-proof and electrically shielded box. Samples were electrically characterized in both d.c. and a.c. regimes using a Keithley 4200SCS semiconductor analyzer. The standard Sawyer-Tower experiment was carried out by using an Agilent DXO-X 3104 digital oscilloscope with a built-in wave generator. This experiment comprised applying a periodic triangular-shaped stimulus and recording the voltage loops data from the oscilloscope. Charge values were obtained from the sensed voltage across a stated capacitance.

Results and Discussion

Film growth, formation, structure and morphology.—On planar Si(100) substrates, the Co_3O_4 and ZrO_2 reference films were grown to the thicknesses of 15.0 ± 1.0 and 32.0 ± 1.0 nm after 250 growth cycles, respectively, according to the XRR measurements (Table I). Thus, the average growth rates of constituent oxides were 0.06 and 0.13 nm/cycle for Co_3O_4 and ZrO_2 films, respectively. Reactor conditions, in particular temperature, reactor volume, but also cycle time and pressure parameters may somewhat affect the film growth rate. In an earlier study on ALD of $Co(acac)_3$ and O_3, the growth rate at 300°C was 0.03 nm/cycle.[61] In another study devoted to ALD of ZrO_2 from $ZrCl_4$ and O_3, the growth rate at 300°C was 0.07 nm/cycle.[46] Both growth rates are smaller than those calculated in this study. As the reactors were different in both cases, the differences in the growth rates might be caused by different reactor chamber pressures and the concentrations of precursor in the carrier gas.

In the case of the nanolaminates, the estimated thickness of a single oxide layer (Table I) is the total measured thickness of the particular oxide in the film divided by the number of these oxide layers. Possible variations in the thicknesses of single oxide layers were not taken into account at this calculation. The growth rate of the metal oxide may be influenced by the substrate material, that is, the metal oxide might grow to the top of the substrate material with different rate compared to the growth on the top of another oxide layer.

As the precursors contained chlorine and carbon, the presence of these two elements as residual impurities in the deposited films is an expected result. Due to the small thickness of the single layers, the impurity contents with ToF-ERDA could only be integrated over the whole nanolaminate. Elemental depth profiles confirm rather low concentrations for impurities – C, Cl and H (Fig. 1). The C, Cl and H contents for $2 \times (Co_3O_4 + ZrO_2) + Co_3O_4$ nanolaminate were 0.5 ± 0.1 at.%, 0.12 ± 0.02 at.%, 1.4 ± 0.2 at.%, respectively. And in the case of $2 \times (ZrO_2 + Co_3O_4) + ZrO_2$ nanolaminate, the C, Cl and H contents were 0.4 ± 0.1 at.%, 0.7 ± 0.1 at.%, 1.0 ± 0.2 at.%. Both

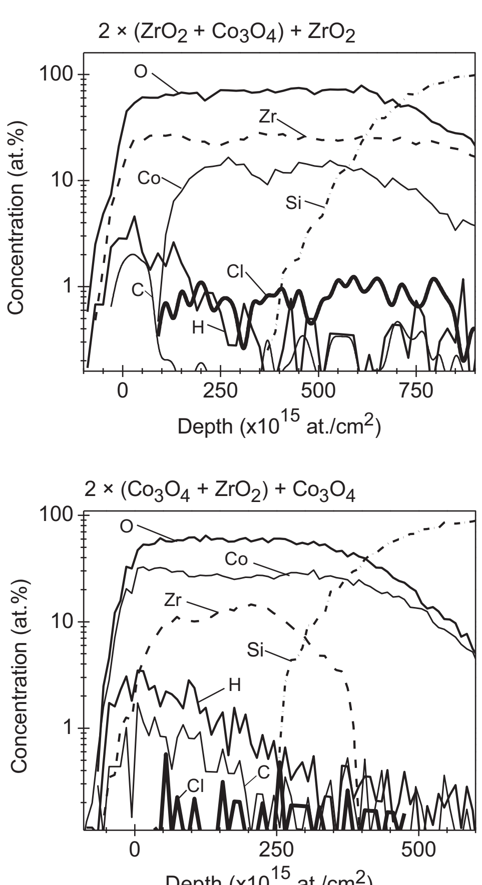

Figure 1. Elemental depth profiles determined by ToF-ERDA for the $2 \times (ZrO_2 + Co_3O_4) + ZrO_2$ (upper panel) and $2 \times (Co_3O_4 + ZrO_2) + Co_3O_4$ (lower panel) nanolaminates in the as-deposited state. The title above the graph indicates the type of nanolaminate.

H and C are concentrated in the first oxide layer or surface. Both H and C concentrations drop drastically deeper in the film stack.

Scanning electron microscope images demonstrated that the surfaces in the case of all four thin film structures (Fig. 2) were quite uniformly covered by grain-like features, which may easily be connected to crystallization, and also indicate that the deposition temperature of 300°C was high enough to cause crystallization in both Co_3O_4 and ZrO_2 thin films. The similarity between those thin film multilayer structures that had the same type of oxide as the topmost layer implies that in the case of nanolaminates, the layers are probably not mixed and the upmost layer is indeed the oxide layer that was defined in the ALD experiment and displayed on the explanatory schematics (Fig. 2). One can also notice that the charging effect has taken place in the case of the ZrO_2 layers, which can be seen by the bright white areas. This effect is more characteristic of the non-conductive (insulating) materials. In Ramesh et al.[62] it has been stated that, in order to be ferroelectric, a material must be insulating (otherwise the mobile charges would screen out the electric polarization).

GIXRD (Fig. 3) confirmed that the reference thin films and ZrO_2-Co_3O_4 nanolaminates were all crystallized already in the as-deposited state. The diffractogram of the reference ZrO_2 thin film (Fig. 3) contained five reflections 111, 200, 220, 311 and 222 at 30.5°, 35.2°, 50.6°, 60.3° and 63.2°, respectively, attributable to cubic ZrO_2 phase (PDF card 00-027-0997). Reflections $\bar{1}11$, 111 and 131 at 28.2°, 31.5°, 59.8°, respectively, could be attributed to the monoclinic ZrO_2 phase (PDF card 00-037-1484). In an earlier study,[46] the formation of both cubic and monoclinic ZrO_2 phases in the thin films deposited at the same temperature and from the same precursors has been described.

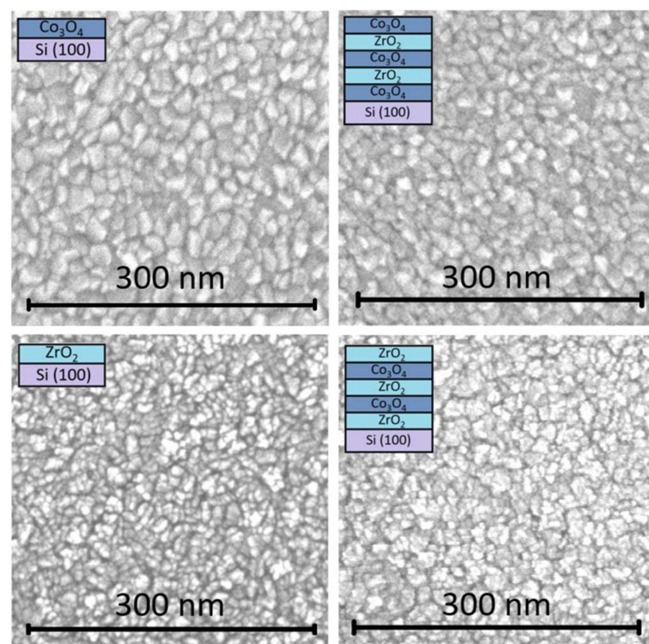

Figure 2. The bird-eye view of the scanning electron microscope images of ZrO_2 and Co_3O_4 thin films and ZrO_2-Co_3O_4 nanolaminates as-deposited with explanatory schematics indicating the order and the amount of layers deposited.

In the diffractogram of the reference Co_3O_4 thin film, six peaks attributable to the 220, 311, 400, 422, 511 ja 440 reflexes from the cubic phase were detected at 31.3°, 36.9°, 44.8°, 55.7°, 59.4° and 65.2° (PDF card 00-042-1467). In an earlier study by Klepper et al.[63] on Co_3O_4, atomic layer deposited at 283°C, the cubic phase has also been detected. While comparing the diffractograms of the nanolaminates one could notice that in the case of the nanolaminate, that had the ZrO_2 as the top-most layer, the peak intensities were noticeably higher and therefore the interlayers must be more ordered compared to the nanolaminate that had Co_3O_4 as the top-most layer. Probably the dominant phase is the cubic ZrO_2 polymorph, although the tetragonal and/or orthorhombic ZrO_2 in the phase composition cannot be completely ruled out.

In STEM images made of both types of nanolaminates (Fig. 4, the leftmost-panel of (a) and (b)), five distinct metal oxide layers grown sequentially on the Si substrate can be seen. Cross-sectional EDX composition profiling of the ZrO_2-Co_3O_4 nanolaminates in the as-deposited state (Fig. 4, 4 small panels of (a) and (b) on the right)

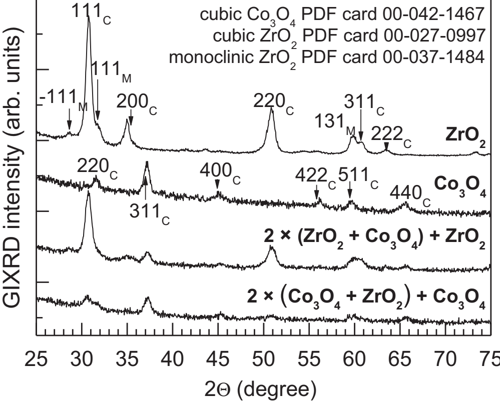

Figure 3. X-ray diffraction patterns from the Co_3O_4 and ZrO_2 thin films and ZrO_2-Co_3O_4 nanolaminates, in the as-deposited state. Miller indexes assigned after crystallization are indicated with "C" for cubic and "M" for monoclinic phase.

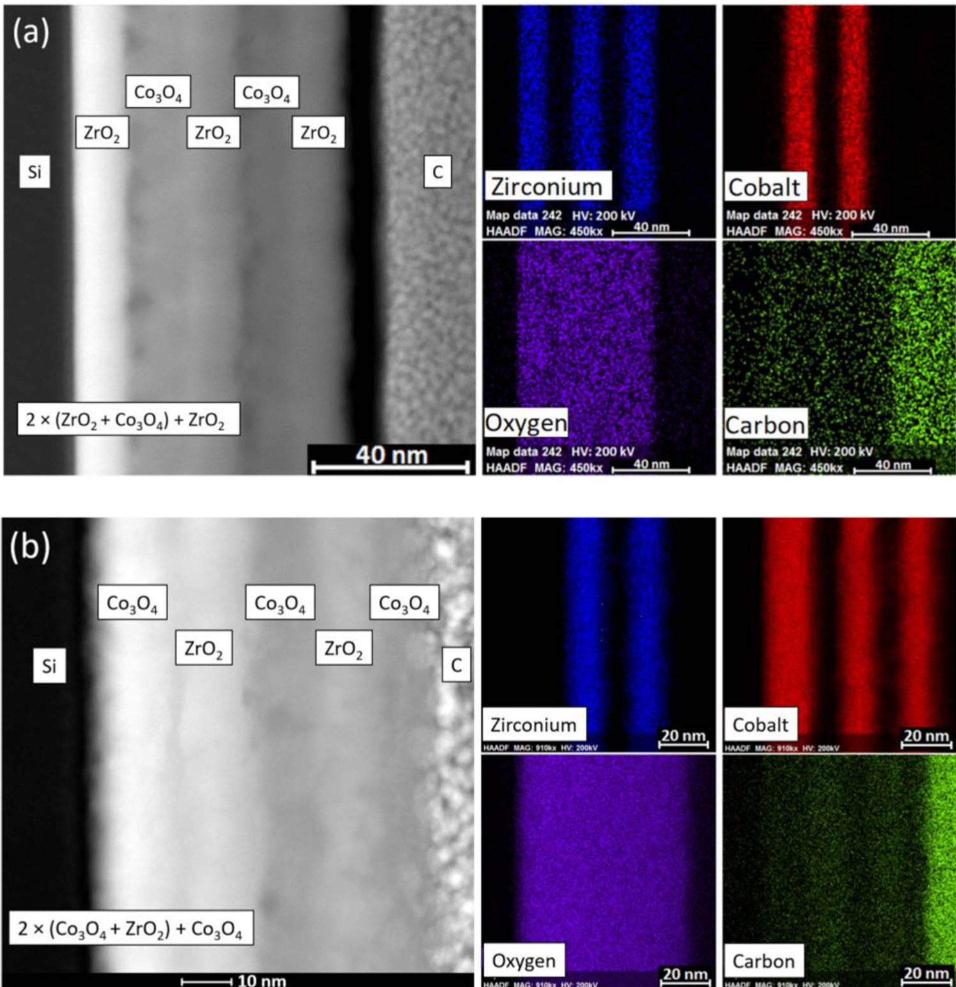

Figure 4. Cross-sectional EDX composition profiling of the (a) $2 \times (ZrO_2 + Co_3O_4) + ZrO_2$ nanolaminate and (b) $2 \times (Co_3O_4 + ZrO_2) + Co_3O_4$ nanolaminate in the as-deposited state. STEM images of the site of interest are displayed on the left panels. The elements detected are indicated by labels and colors displayed on the right panels. Carbon on top of the layers originates from lamellae creation process where it acted as a protective layer.

showed that in the case of the $2 \times (Co_3O_4 + ZrO_2) + Co_3O_4$ nanolaminate, three chemically distinct cobalt-containing and two zirconium-containing layers alternated as expected. In the case of $2 \times (ZrO_2 + Co_3O_4) + ZrO_2$ one can see three alternating zirconium and two cobalt-containing layers. Therefore, the structure of the nanolaminates corresponded to the schematics described in the experimental section. In the case of both nanolaminates, the oxygen signal was detected relatively homogeneously across all five metal oxide layers, as expected. One can also see that the thicknesses of the oxide layers are quite similar indeed, except that in the case of the first layer of $2 \times (Co_3O_4 + ZrO_2) + Co_3O_4$ nanolaminate, where the cobalt oxide occurred slightly thicker compared to the other layers.

Comparison of STEM images and EDX composition profiling made of both types of nanolaminates (Fig. 5) revealed that slight mixing of oxide layers at the interfaces between two oxides has occurred in both cases. Nevertheless, the appearance of distinguishable lattice planes is indicative of ordered structure. In the case of the $2 \times (ZrO_2 + Co_3O_4) + ZrO_2$ nanolaminate the STEM image taken from one other location (Fig. 6) revealed probably a local phenomenon in the form of apparently round features. An apparently similar phenomenon has earlier been observed in the case of atomic layer deposited Ho_2O_3-TiO_2 nanolaminates[64] where Ho_2O_3 and TiO_2 layers were mixed after annealing and the nanolaminate structure was destroyed. If these features were hollow, then the appearance of such regions could be associated with the Kirkendall effect that can arise when two distinct materials are placed in contact to each other and their interdiffusion occurs by a vacancy mechanism. In the context of the present work, however, Kirkendall effect should be considered with caution and this phenomenon therefore would need further investigation. In our study, these round features are likely not voids due to the appearance of distinguishable lattice planes within those round features.

Magnetic and electrical behavior.—In-plane magnetic measurements were performed for as-deposited ZrO_2-Co_3O_4 nanolaminates and reference ZrO_2 and Co_3O_4 thin films. The structures demonstrated ferromagnetic-like behavior at room temperature with saturation magnetization (Fig. 7) and could therefore be described as rather soft ferromagnetics. In the ***M–H*** curves the saturation magnetization values for the ZrO_2 and Co_3O_4 were 3.7×10^{-6} emu and 3.5×10^{-6} emu at 300 K, respectively. One can also notice that the $2 \times (ZrO_2 + Co_3O_4) + ZrO_2$ nanolaminate showed several times higher saturation magnetization (1.7×10^{-5} emu) compared to the other samples. The coercivity values of films were low, ranging from around 24 to 60 Oe (1.9 to 4.8 kA/m), evaluated from their very narrow hysteresis loops.

At first, it might be a bit surprising to see that the nanolaminate that had three layers of ZrO_2 and two layers of Co_3O_4 possessed that much better magnetic polarization compared to the laminate that had one more Co_3O_4 layer and one less ZrO_2 layer. On the other hand, the magnetic behavior of ZrO_2 thin films and nanoparticles has been reported before,[65–68] and the magnetism was largely attributed to the formation and presence of oxygen deficient metastable zirconia phases. In the present study, it was confirmed, that the solid structures

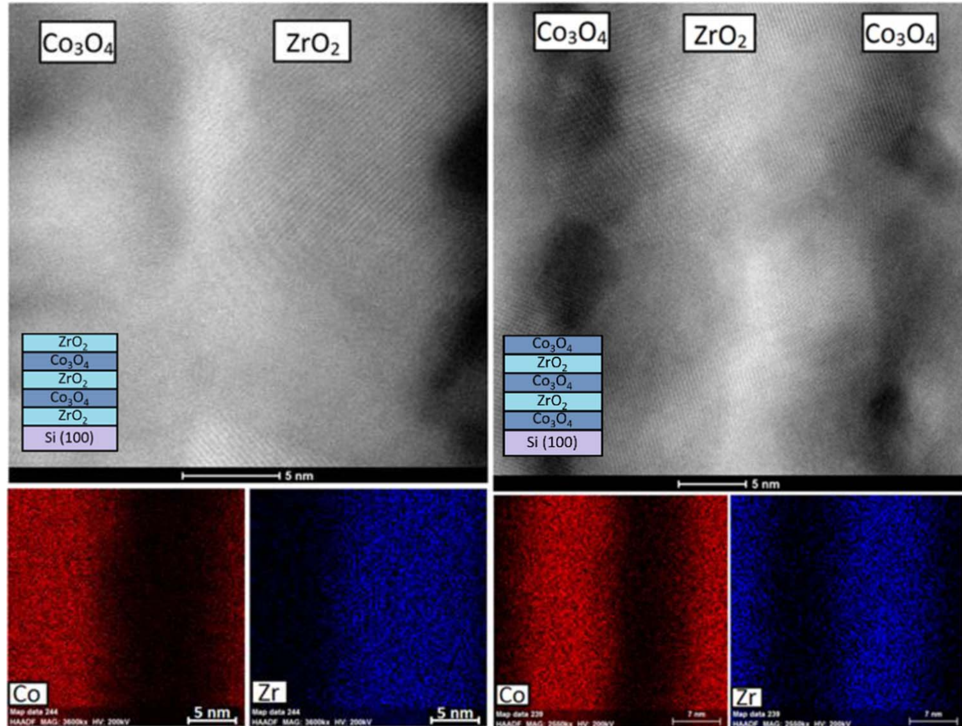

Figure 5. Cross-sectional STEM image and EDX composition profiling taken from the lamellae that were made of the nanolaminates in the as-deposited state. $2 \times (ZrO_2 + Co_3O_4) + ZrO_2$ nanolaminate on the left panels and $2 \times (Co_3O_4 + ZrO_2) + Co_3O_4$ on the right panels.

deposited do not consist of stable crystallographic phases characteristic of perfectly stoichiometric zirconium dioxide. It is likely that the deposited oxides have not been fully oxidized due to the low deposition temperature. Thus, noticeable magnetization is likely caused by a significant contribution from nanocrystalline cubic tetragonal ZrO_2 phase.

From the resistive switching loops (Fig. 8) one can see that both samples show bipolar behavior, but with opposite sign. In the sample Si/TiN/2 × (Co_3O_4 + ZrO_2) + Co_3O_4/Pt (Fig. 8, lower panel) the transition from low to high resistance states (SET)[69,70] occurs for negative voltages between −1.5 and −2.5 V, whereas the transition from high to low resistance state (RESET) occurs for positive voltages in the range of 2.0–3.5 V. It can also be noticed that both transitions are very sharp and currents at the low resistance state are more than one order of magnitude higher than at the OFF state. On the contrary, in the sample Si/TiN/2 × (ZrO_2 + Co_3O_4) + ZrO_2/Pt (Fig. 8, upper panel) SET occurs at positive of about 6 V, whereas RESET occurs at negative voltages in the range of −6–(−8) V, and both transitions are very gradual. Moreover, it is evident that the loops are much narrower.

The opposite sign of the bipolar loops can be related to the different ordering of the multilayers. The conductive filaments in this kind of materials are typically formed due to the accumulation of oxygen vacancies, which cluster, so connecting top and bottom electrodes (set process). Oxygen vacancies are caused due to the migration of negative oxygen ions due to the electric field. RESET process is based on the opposite mechanism: oxygen anions are moved from the metal to the insulator and backfill the vacancies to annihilate the conductive

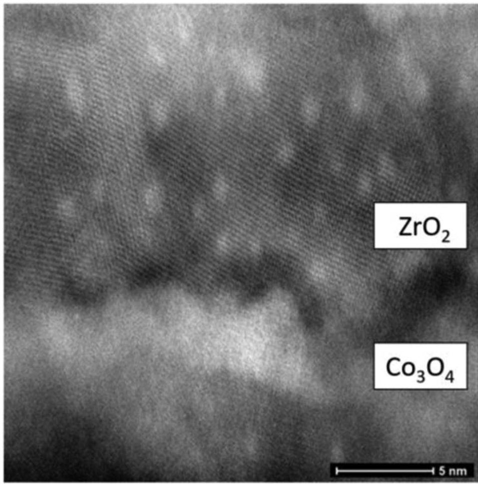

Figure 6. Cross-sectional STEM image taken of the $2 \times (ZrO_2 + Co_3O_4) + ZrO_2$ nanolaminate.

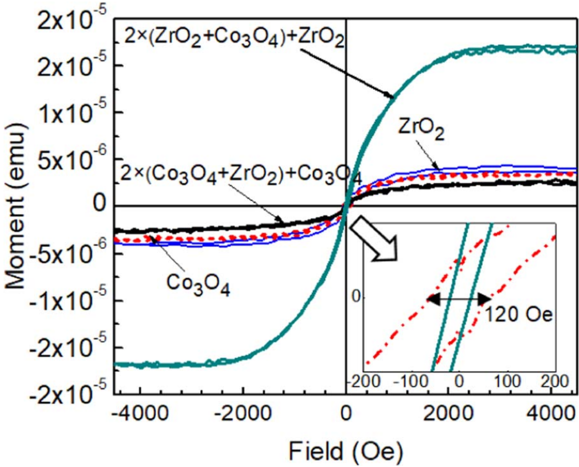

Figure 7. Magnetic moment vs. external magnetic field (***M–H***) curves for the as-deposited ZrO_2-Co_3O_4 nanolaminates and ZrO_2 and Co_3O_4 reference thin films measured at room temperature (300 K).

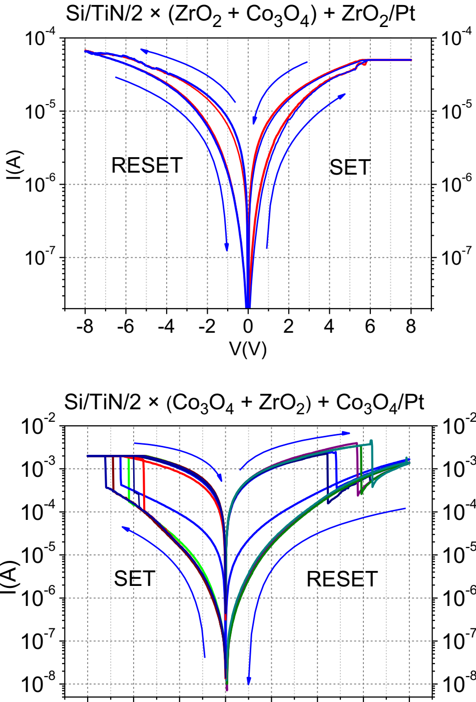

Figure 8. Current-voltage curves measured from the Si/TiN/2 × (ZrO_2 + Co_3O_4) + ZrO_2/Pt (upper panel) and Si/TiN/2 × (Co_3O_4 + ZrO_2) + Co_3O_4/Pt (lower panel) MIM samples.

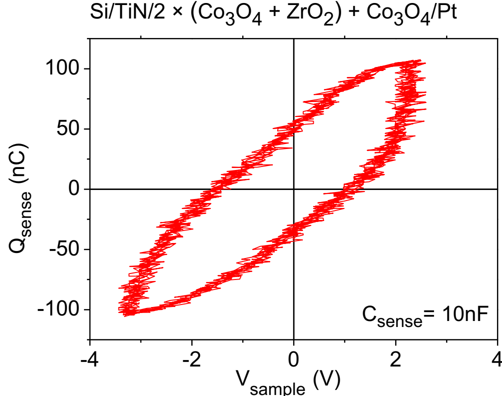

Figure 9. P-V curves of the Si/TiN/2 (Co_3O_4 + ZrO_2) + Co_3O_4/Pt recorded during the Sawyer-Tower measurements. The value of C_{sense} was 10 nF.

path. Therefore, the negative reset voltage indicates that oxygen atoms coming from the top electrode cause the conductive filament oxidation in the adjacent insulator, that is, in the upper dielectric region. That is the case of sample Si/TiN/2 × (ZrO_2 + Co_3O_4) + ZrO_2/Pt, where the upper film is ZrO_2, which is in contact with the top Pt electrode. Pt is reputed to be highly active as an oxygen repository in bipolar switching devices (in contrast, TiN used to be very inactive). In a Si/TiN/2 × (Co_3O_4 + ZrO_2) + Co_3O_4/Pt nanolaminate, where the Co_3O_4 layer is in contact with both of the electrodes, SET and RESET occurs for negative and positive voltages, respectively. Moreover, current loops are wider than for the Si/TiN/2 × (ZrO_2 + Co_3O_4) + ZrO_2/Pt sample. Tentative explanation is that in these samples, the dominant mechanism is the migration of Co cations to the ZrO_2 insulation layer, that is, resistive switching is caused by the electrochemical metallization of the ZrO_2 layer.

The charge polarization – voltage (P-V) hysteresis loops measured during the Sawyer-Tower measurements for the Si/TiN/2 × (Co_3O_4 + ZrO_2) + Co_3O_4/Pt (Fig. 9) and Si/TiN/2 × (ZrO_2 + Co_3O_4) + ZrO_2/Pt (not shown) samples were not promising. The charge polarization was about 55 nC at 0 V for the Si/TiN/2 × (Co_3O_4 + ZrO_2) + Co_3O_4/Pt nanolaminate and 0.6 nC at 0 V for the Si/TiN/2 × (ZrO_2 + Co_3O_4) + ZrO_2/Pt nanolaminate. The shape of those loops is typical to a lossy dielectric and therefore not characteristic to a ferroelectric material.[71]

In general, the films grown in the present study performed as moderately insulating dielectric metal oxides. The capacitance measurements revealed that the oxide layers in metal-oxide-nitride exhibited dielectric dispersion behavior rather common in high-permittivity oxide materials. The permittivity values measured in these laminates evidently exceeded 30–35 at measurement frequencies ranging from 1 to 10 kHz (Fig. 10), which can be explained by considerable contribution of metastable crystalline ZrO_2 phases in the films. However, in the laminate with structure of 2 × (Co_3O_4 + ZrO_2) + Co_3O_4 the apparent permittivity value at relatively low frequencies approached values as high as 100, which is most likely due to high leakage in the films and concurrent interface or space charge polarization.

In the five-layer nanolaminates investigated in the present study, the dominance of metastable ZrO_2 polymorphs (cubic/tetragonal) over the monoclinic phase appeared somewhat clearer compared to that observed earlier in ZrO_2/Co_3O_4 double layers,[59] decided on the basis of XRD results. Concurrently, the saturation magnetization tended to be higher, although differences in the magnetization hysteresis width occurred insignificant. Charge polarization in the capacitor structures did not differ essentially in nanolaminates and double layers. At the same time, nanolaminates in the present study tended to demonstrate somewhat wider window between high and low resistance states, as

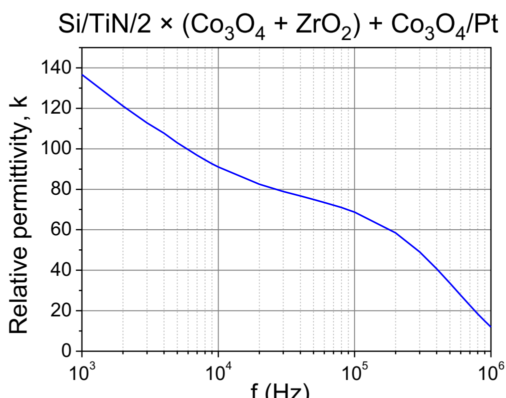

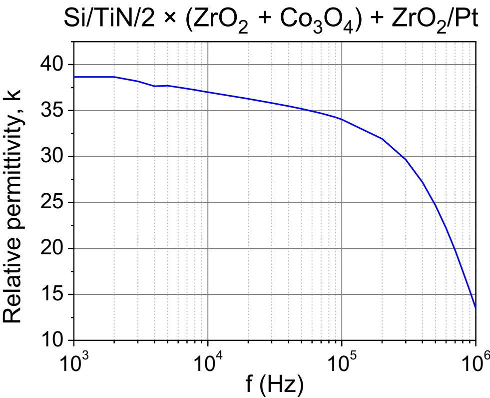

Figure 10. Permittivity dispersion in the nanolaminate films with structures denoted by labels.

measured in the resistive switching regime. The high resistance state was thereby realized at lower current values, which may expected to be advantageous when aiming at lowered power consumption during the information reading process, if such materials were applied in memristor cells.

Summary

ZrO_2-Co_3O_4 nanolaminates were grown by atomic layer deposition. The films consisting of distinct metal oxide layers were formed. The performance of the laminate films was dependent on the relative content of constituent oxide layers. The structure that consisted alternately of three ZrO_2 and two Co_3O_4 layers showed higher magnetization compared to the structure that consisted alternately of three Co_3O_4 and two ZrO_2 layers. All studied structures exhibited characteristics that are inherent to ferro- or ferrimagnetic materials like saturation magnetization and non-linear relationship between magnetic moment and external magnetic field. Electrical measurements revealed formation of significant polarization versus external field loops, probably markedly influenced by interfacial polarization and both samples showed bipolar behavior in resistive switching regime, although with an opposite sign.

Acknowledgments

The authors of the paper are thankful to Alma-Asta Kiisler for the technical assistance in sample preparation, to Jekaterina Kozlova for sharing her support and knowledge in connection with the lamellae creation process, to Peeter Ritslaid for his support in XRF studies and to Dr. Aarne Kasikov for depositing the electrodes and ellipsometric measurements. The study was partially supported by the European Regional Development Fund project "Emerging orders in quantum and nanomaterials" (TK134), Estonian Academy of Sciences (SLTFYPROF), Estonian Research Agency (IUT2-24, PRG4) and Spanish Ministry of Economy and Competitiveness (TEC2017-84321-C4-2-R) with support of Feder funds.

ORCID

Helina Seemen https://orcid.org/0000-0002-4850-0851
Kristjan Kalam https://orcid.org/0000-0001-5934-1860
Timo Sajavaara https://orcid.org/0000-0003-2235-7441
Salvador Dueñas https://orcid.org/0000-0002-2328-1752
Helena Castán https://orcid.org/0000-0002-3874-721X
Raivo Stern https://orcid.org/0000-0002-6724-9834
Kaupo Kukli https://orcid.org/0000-0002-5821-0364
Aile Tamm https://orcid.org/0000-0002-0547-0824

References

1. J. Riegel, H. Neumann, and H.-M. Wiedenmann, "Exhaust gas sensors for automotive emission control," *Solid State Ion*. **152–153**, 783 (2002).
2. G. Lu, N. Miura, and N. Yamazoe, "High-temperature hydrogen sensor based on stabilized zirconia and a metal oxide electrode," *Sens. Actuators B Chem.*, **35**, 130 (1996).
3. P. D. L. Mercera, J. G. van Ommen, E. B. M. Doesburg, A. J. Burggraaf, and J. R. H. Ross, "Zirconia as a support for catalysts: influence of additives on the thermal stability of the porous texture of monoclinic zirconia," *Appl. Catal.*, **71**, 363 (1991).
4. J. Ftouni, A. Muñoz-Murillo, A. Goryachev, J. P. Hofmann, E. J. M. Hensen, L. Lu, C. J. Kiely, P. C. A. Bruijnincx, and B. M. Weckhuysen, "ZrO_2 is preferred over TiO_2 as support for the Ru-catalyzed hydrogenation of levulinic acid to γ-valerolactone," *ACS Catal.*, **6**, 5462 (2016).
5. D. Zhu and R. A. Miller, "Thermal conductivity and elastic modulus evolution of thermal barrier coatings under high heat flux conditions," *J. Therm. Spray Tech.*, **9**, 175 (2000).
6. U. Schulz and M. Schmücker, "Microstructure of ZrO_2 thermal barrier coatings applied by EB-PVD," *Mater. Sci. Eng.: A*, **276**, 1 (2000).
7. S. B. Ogale, R. D. Vispute, and R. R. Rao, "Pulsed excimer laser deposition $Y_1Ba_2Cu_3O_{7-x}$ superconductor films on silicon with laser-deposited Y-ZrO_2 buffer layer," *Appl. Phys. Lett.*, **57**, 1805 (1990).
8. H. Schmidt, K. Hradil, W. Hösler, and W. Wersing, "Epitaxial $YBa_2Cu_3O_x$ thin films on sapphire using a Y-stabilized ZrO_2 buffer layer," *Appl. Phys. Lett.*, **59**, 222 (1991).
9. H. J. Cho, Y. D. Kim, D. S. Park, E. Lee, C. H. Park, J. S. Jang, K. B. Lee, H. W. Kim, Y. J. Ki, I. K. Han, and Y. W. Song, "New TIT capacitor with $ZrO_2/Al_2O_3/ZrO_2$ dielectrics for 60 nm and below DRAMs," *Solid-State Electron.*, **51**, 1529 (2007).
10. K. Black, H. C. Aspinall, A. C. Jones, K. Przybylak, J. Bacsa, P. R. Chalker, S. Taylor, C. Z. Zhao, S. D. Elliott, and A. Zydor P. N. Heys, "Deposition of ZrO_2 and HfO_2 thin films by liquid injection MOCVD and ALD using ansa-metallocene zirconium and hafnium precursors," *J. Mater. Chem.*, **18**, 4561 (2008).
11. T. S. Kalkur and Y. C. Lu, "Electrical characteristics of ZrO_2-based metal-insulator-semiconductor structures on p-Si," *Thin Solid Films*, **207**, 193 (1992).
12. S. Monaghan, K. Cherkaoui, É. O'Connor, V. Djara, P. K. Hurley, L. Oberbeck, E. Tois, L. Wilde, and S. Teichert, "TiN/ZrO_2/Ti/Al metal-insulator-metal capacitors with subnanometer CET using ALD-deposited ZrO_2 for DRAM applications," *IEEE Electron Device Lett.*, **30**, 219 (2009).
13. D. Panda and T.-Y. Tseng, "Growth, dielectric properties, and memory device applications of ZrO_2 thin films," *Thin Solid Films*, **531**, 1 (2013).
14. C. Y. Lin, C.-Y. Wu, C.-Y. Wu, T.-C. Lee, F.-L. Yang, C. Hu, and T.-Y. Tseng, "Effect of top electrode material on resistive switching properties of ZrO_2 film memory devices," *IEEE Electron Device Lett.*, **28**, 366 (2007).
15. Y. Li, S. Long, M. Zhang, Q. Liu, L. Shao, S. Zhang, Y. Wang, Q. Zuo, S. Liu, and M. Liu, "Resistive switching properties of Au/ZrO_2/Ag structure for low-voltage nonvolatile memory applications," *IEEE Electron Device Lett.*, **31**, 117 (2010).
16. Z. Wen, L. Zhu, W. Mei, L. Hu, Y. Li, L. Sun, H. Cai, and Z. Ye, "Rhombus-shaped Co_3O_4 nanorod arrays for high-performance gas sensor," *Sens. Actuators B Chem.*, **186**, 172 (2013).
17. S. Vetter, S. Haffer, T. Wagner, and M. Tiemann, "Nanostructured Co_3O_4 as a CO gas sensor: temperature-dependent behavior," *Sens. Actuators B Chem.*, **206**, 133 (2015).
18. S. Fujita, K. Suzuki, and T. Mori, "Preparation of high-performance Co_3O_4 catalyst for hydrocarbon combustion from Co-containing hydrogarnet," *T. Catalysis Letters*, **86**, 139 (2003).
19. M. R. Mate, M. Shirai, and C. V. Rode, "Heterogeneous Co_3O_4 catalyst for selective oxidation of aqueous veratryl alcohol using molecular oxygen," *Catal. Commun.*, **33**, 66 (2013).
20. W. Y. Li, L. N. Xu, and Chen J, "Co_3O_4 nanomaterials in lithium-ion batteries and gas sensors," *Adv. Funct. Mater.*, **15**, 851 (2005).
21. Q. Liao, N. Li, S. Jin, G. Yang, and C. Wang, "All-solid-state symmetric supercapacitor based on Co_3O_4 nanoparticles on vertically aligned graphene," *ACS Nano*, **9**, 5310 (2015).
22. M. Moulapanah-Konaroi, M. Aliahmad, and H. Saravani, "Fabrication of superhydrophobic surface by Co_3O_4 nanoparticles," *Indian J. Phys.*, **87**, 211 (2013).
23. Z. Guo and W. Liu, "Superhydrophobic spiral Co_3O_4 nanorod arrays," *Appl. Phys. Lett.*, **90**, 193108 (2007).
24. J. Chen, X. Wu, and A. Selloni, "Electronic structure and bonding properties of cobalt oxide in the spinel structure," *Phys. Rev. B*, **83**, 245204 (2011).
25. W. Hu, L. Zou, X. Lin, C. Gao, Y. Guo, and D. Bao, "Unipolar resistive switching effect and mechanism of solution-processed spinel Co_3O_4 thin films," *Mater. Des.*, **103**, 230 (2016).
26. X. Gao, H. Guo, Y. Xia, J. Yin, and Z. Liu, "Unipolar resistive switching characteristics in Co_3O_4 films," *Thin Solid Films*, **519**, 450 (2010).
27. V. R. Shinde, S. B. Mahadik, T. P. Gujar, and C. D. Lokhande, "Supercapacitive cobalt oxide (Co_3O_4) thin films by spray pyrolysis," *Appl. Surf. Sci.*, **252**, 7487 (2006).
28. G. Adamopoulos, S. Thomas, P. H. Wöbkenberg, D. D. C. Bradley, M. A. McLachlan, and T. D. Anthopoulos, "High-mobility low-voltage ZnO and Li-doped ZnO transistors based on ZrO_2 high-k dielectric grown by spray pyrolysis in ambient air," *Adv. Mater.*, **23**, 1894 (2011).
29. S. Z. Abbas, A. A. Aboud, M. Irfan, and S. Alam, "Effect of substrate temperature on structure and optical properties of Co_3O_4 films prepared by spray pyrolysis technique," *IOP Conf. Ser. Mater. Sci. Eng.*, **60**, 012058 (2014).
30. T. S. Jeon, J. M. White, and D. L. Kwong, "Thermal stability of ultrathin ZrO_2 films prepared by chemical vapor deposition on Si(100)," *Appl. Phys. Lett.*, **78**, 368 (2001).
31. C. M. Perkins, B. B. Triplett, P. C. McIntyre, K. C. Saraswat, S. Haukka, and M. Tuominen, "Electrical and materials properties of ZrO_2 gate dielectrics grown by atomic layer chemical vapor deposition," *Appl. Phys. Lett.*, **78**, 2357 (2001).
32. N. Bahlawane, E. F. Rivera, K. Kohse-Höinghaus, A. Brechling, and U. Kleineberg, "Characterization and tests of planar Co_3O_4 model catalysts prepared by chemical vapor deposition," *Appl. Catal. B Environ.*, **53**, 245 (2004).
33. D. Barreca, C. Massignan, S. Daolio, M. Fabrizio, C. Piccirillo, L. Armelao, and E. Tondello, "Composition and microstructure of cobalt oxide thin films obtained from a novel cobalt(II) precursor by chemical vapor deposition," *Chem. Mater.*, **13**, 588 (2001).
34. Z.-W. Fu, Y. Wang, Y. Zhang, and Q.-Z. Qin, "Electrochemical reaction of nanocrystalline Co_3O_4 thin film with lithium," *Solid State Ion.*, **170**, 105 (2004).
35. J. Zhu and Z. G. Liu, "Structure and dielectric properties of ultra-thin ZrO_2 films for high-*k* gate dielectric application prepared by pulsed laser deposition," *Appl. Phys. A*, **78**, 741 (2004).
36. W.-C. Liu, D. Wu, A.-D. Li, H.-Q. Ling, Y.-F. Tang, and N.-B. Ming, "Annealing and doping effects on structure and optical properties of sol–gel derived ZrO_2 thin films," *Appl. Surf. Sci.*, **191**, 181 (2002).
37. H. Tototzintle-Huitle, E. Prokhorov, A. Mendoza-Galván, J. E. Urbina, and J. González-Hernández, "Study of the formation of Co_3O_4 thin films using sol–gel method," *J. Phys. Chem. Solids*, **64**, 975 (2003).

38. K. Balachander, S. Arulkumaran, H. Ishikawa, K. Baskar, and T. Egawa, "Studies on electron beam evaporated ZrO_2/AlGaN/GaN metal–oxide–semiconductor high-electron-mobility transistors," *Phys. Status Solidi A*, **202**, R16 (2005).
39. J. Wöllenstein, M. Burgmair, G. Plescher, T. Sulima, J. Hildenbrand, H. Böttner, and I. Eisele, "Cobalt oxide based gas sensors on silicon substrate for operation at low temperatures," *Sens. Actuators B Chem.*, **93**, 442 (2003).
40. M. Cassir, F. Goubin, C. Bernay, P. Vernoux, and D. Lincot, "Synthesis of ZrO_2 thin films by atomic layer deposition: growth kinetics, structural and electrical properties," *Appl. Surf. Sci.*, **193**, 120 (2002).
41. M. Putkonen, J. Niinistö, K. Kukli, T. Sajavaara, M. Karppinen, H. Yamauchi, and L. Niinistö, "ZrO_2 thin films grown on silicon substrates by atomic layer deposition with $Cp_2Zr(CH_3)_2$ and water as precursors," *Chem. Vap. Depos.*, **9**, 207 (2003).
42. W.-H. Nam and S.-W. Rhee, "Atomic layer deposition of ZrO_2 thin films using dichlorobis[bis-(trimethylsilyl)amido]zirconium and water," *Chem. Vap. Depos.*, **10**, 201 (2004).
43. J. Niinistö, A. Rahtu, M. Putkonen, M. Ritala, M. Leskelä, and L. Niinistö, "In situ quadrupole mass spectrometry study of atomic-layer deposition of ZrO_2 using $Cp_2Zr(CH_3)_2$ and water," *Langmuir*, **21**, 7321 (2005).
44. K. B. Klepper, O. Nilsen, and H. Fjellvåg, "Growth of thin films of Co_3O_4 by atomic layer deposition," *Thin Solid Films*, **515**, 7772 (2007).
45. B. Han, J.-M. Park, K. H. Choi, W.-K. Lim, T. R. Mayangsari, W. Koh, and W.-J. Lee, "Atomic layer deposition of stoichiometric Co_3O_4 films using bis(1,4-di-iso-propyl-1,4-diazabutadiene) cobalt," *Thin Solid Films*, **589**, 718 (2015).
46. K. Kukli, M. Kemell, J. Köykkä, K. Mizohata, M. Vehkamäki, M. Ritala, and M. Leskelä, "Atomic layer deposition of zirconium dioxide from zirconium tetrachloride and ozone," *Thin Solid Films*, **589**, 597 (2015).
47. W. F. A. Besling, E. Young, T. Conard, C. Zhao, R. Carter, W. Vandervorst, M. Caymax, S. De Gendt, M. Heyns, J. Maes, M. Tuominen, and S. Haukka, "Characterisation of ALCVD Al_2O_3–ZrO_2 nanolaminates, link between electrical and structural properties," *J. Non-Cryst. Solids*, **303**, 123 (2002).
48. J. Meyer, P. Görrn, F. Bertram, S. Hamwi, T. Winkler, H. -H. Johannes, T. Weimann, P. Hinze, T. Riedl, and W. Kowalsky, "Al_2O_3/ZrO_2 nanolaminates as ultrahigh gas-diffusion barriers—a strategy for reliable encapsulation of organic electronics," *Adv. Mater.*, **21**, 1845 (2009).
49. Z. Tang, X. Zhu, H. Xu, Y. Xia, J. Yin, Z. Liu, A. Li, and F. Yan, "Impact of the interfaces in the charge trap layer on the storage characteristics of ZrO_2/Al_2O_3 nanolaminate-based charge trap flash memory cells," *Mater. Lett.*, **92**, 21 (2013).
50. G. Balakrishnan, A. Wasy, H. S. Ho, P. Sudhakara, S. I. Bae, and J. I. Song, "Study of Al_2O_3/ZrO_2 (5 nm/20 nm) nanolaminate composite," *Compos. Res.*, **26**, 60 (2013).
51. L. Zhong, F. Chen, S. A. Campbell, and W. L. Gladfelter, "Nanolaminates of zirconia and silica using atomic layer deposition," *Chem. Mater.*, **16**, 1098 (2004).
52. K. Kukli, J. Ihanus, M. Ritala, and M. Leskelä, "Properties of Ta_2O_5-based dielectric nanolaminates deposited by atomic layer epitaxy," *J. Electrochem. Soc.*, **144**, 300 (1997).
53. H. Zhang and R. Solanki, "Atomic layer deposition of high dielectric constant nanolaminates," *J. Electrochem. Soc.*, **148**, F63 (2001).
54. H. Kim, P. C. McIntyre, and K. C. Saraswat, "Microstructural evolution of ZrO_2–HfO_2 nanolaminate structures grown by atomic layer deposition," *J. Mater. Res.*, **19**, 643 (2004).
55. A. Tamm, M. Heikkilä, M. Kemell, J. Kozlova, K. Kukli, V. Sammelselg, M. Ritala, and M. Leskelä, "Atomic layer deposition and characterization of zirconium oxide–erbium oxide nanolaminates," *Thin Solid Films*, **519**, 666 (2010).
56. I. Jõgi, A. Tamm, K. Kukli, M. Kemell, J. Lu, T. Sajavaara, M. Ritala, and M. Leskelä, "Investigation of ZrO_2–Gd_2O_3 based high-*k* materials as capacitor dielectrics," *J. Electrochem. Soc.*, **157**, G202 (2010).
57. C. N. Ginestra, R. Sreenivasan, A. Karthikeyan, S. Ramanathan, and P. C. McIntyre, "Atomic layer deposition of Y_2O_3/ZrO_2 nanolaminates a route to ultrathin solid-state electrolyte membranes," *Electrochem. Solid-State Lett.*, **10**, B161 (2007).
58. P. Wiecinska, L. Skrzos, and N. Prokurat, "New route for processing of multilayer Al_2O_3-Co_3O_4 materials through gelcasting," *J. Eur. Ceram. Soc.*, **37**, 1627 (2017).
59. K. Kalam, H. Seemen, M. Mikkor, T. Jõgiaas, P. Ritslaid, A. Tamm, K. Kukli, A. Kasikov, J. Link, R. Stern, S. Dueñas, H. Castán, and H. García, Electrical and magnetic properties of atomic layer deposited cobalt oxide and zirconium oxide nanolaminates (submitted to Thin Solid Films).
60. T. Arroval, L. Aarik, R. Rammula, V. Kruusla, and J. Aarik, "Effect of substrate-enhanced and inhibited growth on atomic layer deposition and properties of aluminium-titanium oxide films," *Thin Solid Films*, **600**, 120 (2016).
61. V. Pore, M. Dimri, H. Khanduri, R. Stern, J. Lu, L. Hultman, K. Kukli, M. Ritala, and M. Leskelä, "Atomic layer deposition of ferromagnetic cobalt doped titanium oxide thin films," *Thin Solid Films*, **519**, 3318 (2011).
62. R. Ramesh and N. A. Spaldin, "Multiferroics: progress and prospects in thin films," *Nature Materials*, **6**, 22 (2007).
63. K. B. Klepper, O. Nilsen, and H. Fjellvåg, "Growth of thin films of Co_3O_4 by atomic layer deposition," *Thin Solid Films*, **515**, 7772 (2007).
64. K. Kukli, J. Lu, J. Link, M. Kemell, E. Puukilainen, M. Heikkilä, R. Hoxha, L. Hultman A.Tamm, R. Stern, M. Ritala, and M. Leskelä, "Holmium and titanium oxide nanolaminates by atomic layer deposition," *Thin Solid Films*, **565**, 165 (2014).
65. F. Máca, J. Kudrnovský, V. Drchal, and G. Bouzerar, "Magnetism without magnetic impurities in ZrO_2 oxide," *Applied Physics Letters*, **92**, 212503 (2008).
66. S. Ning, P. Zhan, Q. Xie, Z. Li, and Z. Zhang, "Room-temperature ferromagnetism in un-doped ZrO_2 thin films," *J. Phys. Appl. Phys.*, **46**, 445004 (2013).
67. M. A. Rahman, S. Rout, J. P. Thomas, D. McGillivray, and K. T. Leung, "Defect-rich dopant-free ZrO_2 nanostructures with superior dilute ferromagnetic semiconductor properties," *J. Am. Chem. Soc.*, **138**, 11896 (2016).
68. M. C. Dimri, H. Khanduri, H. Kooskora, M. Kodu, R. Jaaniso, I. Heinmaa, A. Mere, J. Krustok, and R. Stern, "Room-temperature ferromagnetism in Ca and Mg stabilized cubic zirconia bulk samples and thin films prepared by pulsed laser deposition," *J. Phys. Appl. Phys.*, **45**, 475003 (2012).
69. D. Ielmini, "Resistive switching memories based on metal oxides: mechanisms, reliability and scaling," *Semicond. Sci. and Technol.*, **31**, 063002 (2016).
70. F. Pan, C. Chen, Z.-S. Wang, Y.-C. Yang, J. Yang, and F. Zeng, "Nonvolatile resistive switching memories-characteristics, mechanisms and challenges," *Prog. Nat. Sci. Mater. Int.*, **20**, 1 (2010).
71. J. F. Scott, "Ferroelectrics go bananas," *J. Phys. Condens. Matter*, **20**, 021001 (2008).